Mineralogy and Petrology (2021) 115:137–147
https://doi.org/10.1007/s00710-020-00730-y

ORIGINAL PAPER

SFCA-II type $Ca_{2.46}Fe^{3+}_{8.57}Fe^{2+}_{0.52}Al_{5.45}O_{24}$ – an improved structural model for an iron-ore sinter phase

Volker Kahlenberg[1] · Hannes Krüger[1] · Martina Tribus[1] · Benedikt Anwander[1]

Received: 27 October 2020 / Accepted: 24 November 2020 / Published online: 5 January 2021

Abstract

Single crystals of SFCA-II with composition $Ca_{2.46}Fe^{3+}_{8.57}Fe^{2+}_{0.52}Al_{5.45}O_{24}$ have been obtained from synthesis experiments in the temperature range between 1300 and 1200 °C. Diffraction experiments at ambient conditions yielded the following basic crystallographic data: space group $P\,\bar{1}$, $a = 10.3016(4)$ Å, $b = 10.4656(4)$ Å, $c = 17.9553(6)$ Å, $\alpha = 90.062(3)$, $\beta = 89.977(3)°$, $\gamma = 109.510(3)°$, $V = 1824.66(12)$ Å^3, $Z = 4$. Structure determination and subsequent least-squares refinements resulted in a residual of $R(|F|) = 0.0349$ for 7406 independent reflections and 773 parameters. Site occupancy refinements on the 35 octahedral (M) and tetrahedral (T) positions in the asymmetric unit were aided by crystallochemical considerations and the assumption of charge balance between the cations and anions. The derived formula compares well with the outcome of electron microprobe studies. The crystal structure of SFCA-II shows the typical features of the SFCA-family. It can be built from an alternating sequence of two different types of fundamental layers. For SFCA-II, they are oriented parallel to (100). Layer-type I is solely based on $[MO_6]$-octahedra (M: Ca, Fe^{3+}, Al) forming individual five polyhedra wide bands. Within a single band, the octahedra share common edges. Layer-type II, on the other hand, contains $[MO_6]$-octahedra as well as $[TO_4]$-tetrahedra (T: Al, Fe^{3+}, Fe^{2+}). By corner sharing each $[MO_6]$-group is linked to two adjacent tetrahedra into $[MT_2O_{12}]$-clusters or "winged octahedra". Linkage between neighboring strips of these moieties is provided by additional $[TO_4]$-tetrahedra arranged in *vierer* single-chains. Our investigation rectifies previous studies on SFCA-II where wrong atomic coordinates have been published.

Keywords SFCA-II · Cation distribution · Iron-ore sinter · Crystal structure

Introduction

Agglomeration of iron-ore fines with particles sizes less than 6.3 mm in a sinter plant is an integral part of the iron-making process (Jankovic 2015; Fernandez-Gonzalez et al. 2017). In a series of complex reactions between 1250 and 1350 °C, porous semi-molten, centimeter-sized aggregates are formed containing ore particles (hematite and magnetite, constituting 40 to 70% vol.) cemented by a matrix of Ca-rich ferrites (20 to 50% vol.), up to 10% vol. quenched melt (glass) and about 10% vol. calcium silicates such as larnite (β-Ca_2SiO_4) (Patrick and Lovel 2001). For the Ca-rich ferrites that contain some silica and alumina the acronym SFCA is used in the literature, which stands for **S**ilico-**F**errites of **C**alcium and **A**luminum. They represent complex solid-solutions in the system $CaO(+MgO)$-Al_2O_3-$Fe_2O_3(+FeO)$-SiO_2 and appear via reactions between earlier-formed, lower-temperature ferrites such as brownmillerite ($Ca_2(Fe_{1-x}Al_x)_2O_5$), $CaFe_2O_4$, or $CaFe_4O_7$ and gangue minerals containing Al_2O_3 and SiO_2 (Webster et al. 2012). Technologically, the SFCA phases act as the primary binder that keeps the sinters intact in order to withstand the loads in a blast furnace (Nicol et al. 2018). Furthermore, when compared with the iron-ore raw materials, the newly formed SFCA compounds possess a superior reducibility and low reduction degradation, both of which are important factors for the productivity and efficiency of the blast furnace (Webster et al. 2012).

From a chemical and structural point of view, four principal members of the SFCA-family have been distinguished so far, which are labeled by roman numbers: SFCA (Hamilton et al. 1989), SFCA-I (Mumme et al. 1998), SFCA-II (Mumme 2003) and SFCA-III (Zöll et al. 2018), respectively. Though

Editorial handling: N. V. Chukanov

✉ Volker Kahlenberg
volker.kahlenberg@uibk.ac.at

[1] Institute of Mineralogy and Petrography, University of Innsbruck, Innrain 52, A-6020 Innsbruck, Austria

representing different phases with unique sets of lattice parameters, they are closely related to each other. SFCA, SFCA-I and SFCA-III, for example, form a homologous or polysomatic series with general composition $M_{14+6n}O_{20+8n}$, where these three phases represent the members with $n = 0$, 1 and 2, respectively. SFCA-II in turn can be described as an intermediate between SFCA and SFCA-I. Furthermore, the crystal structures of the synthetic SFCA compounds show a relationship with the aenigmatite or sapphirine group of minerals (Merlino and Zvyagin 1998; Mumme 1988; Zvyagin and Merlino 2003) and can be classified by the same approach of stacking sequences of pyroxene (P) and spinel (S) modules.

To date, SFCA (the low-Fe form believed to show a more prismatic morphology) as well as SFCA-I (an iron-richer, low-Si form with a platy habitus) have been found in industrial samples in larger quantities. SFCA-II, on the other hand, was reported to be present in South African sinters (Van den Berg and de Villiers 2008). In the course of an ongoing research project on the crystal chemistry and stability of the SFCA's we came to the conclusion that the published atomic coordinates of SFCA-II (Mumme 2003) may contain errors as calculations of the derived bond lengths of the octahedral coordination environments resulted in individual (Fe,Al)-O distances as low as 1.536 Å. Given that reliable phase quantification by powder X-ray diffraction (PXRD) using the Rietveld method is first and foremost dependent on accurate crystal structure data for the individual constituents it was deemed necessary to re-examine the crystal structure of SFCA-II in more detail. Alongside with a correction of basic crystallographic data the present contribution is also a further step towards an increased accuracy in quantification of iron-ore sinters by PXRD, which still is a challenging task (de Villiers and Verryn 2008).

Experimental details

According to own preliminary studies, single crystals of SFCA-II were obtained from synthesis experiments using mixtures with molar ratio CaO: Fe_2O_3: Al_2O_3 = 1: 1: 1. Starting materials for a total of 2 g were Fe_2O_3 (99.9%, Alfa Aesar), γ-Al_2O_3 (99,997%, Alfa Aesar), and $CaCO_3$ (99.995% Merck). The reagents were dried at 300 °C for 24 h and subsequently checked for impurities using PXRD before weighing on an analytical balance. A planetary mill operated at 600 rpm was used for homogenization for 45 min under ethanol. The resulting slurry was dried for 12 h at 50 °C to remove the alcohol completely, manually re-homogenized in an agate mortar and finally stored in a desiccator. Subsequently, the powder was pressed into pellets each of about 0.5 g in weight, 12 mm in diameter and a thickness of about 2 mm. In the next step, the pellets were sintered in air using an open Pt-crucible placed in a resistance heated chamber furnace. Samples were fired from 20 °C (with a ramp of 120 °C/h) to the maximum temperature of 1300 °C followed by cooling with a rate of 5 °C/h to 1200 °C where the crucible was immediately quenched in air. Weight losses were determined from weight differences before and after heating.

PXRD data for phase analysis have been acquired with a Stoe MP diffractometer system (STOE & Cie GmbH, Darmstadt, Germany) configured in Bragg-Brentano geometry in combination with a Mythen 1 K detector (Dectris Ltd., Baden-Daettwil, Switzerland). The device is equipped with a primary-beam Ge(111) monochromator yielding $K\alpha_1$ radiation only. In order to avoid fluorescence problems due to the iron containing samples the diffraction studies were performed with a cobalt tube operated at 40 kV and 30 mA. Data were collected at ambient temperature over a 2θ range between 5 ° and 120 ° and a step size of 0.015 ° 2θ. The total measurement time was about 48 h. Evaluation of the phase content was performed with the 2018 release of the PDF-4+ Powder Diffraction File database of the International Centre for Diffraction Data (Gates-Rector and Blanton 2019).

To obtain the chemical compositions of the observed phases and to visualize the phase relations in the experiments, parts of the sinter-tablets were embedded in epoxy resin, polished with diamond paste (10, 5 and 1 μm grain size) and finally sputter-coated with carbon. Electron microprobe analysis (EMPA) in wavelength-dispersive mode was performed using a JEOL JXA SUPERPROBE 8100. Measurements were accomplished with an acceleration voltage of 15 kV, a beam current of 10 nA and counting times of 20 s (on peaks) and 10 s (for background on each side of the peaks), respectively. Depending on the size, at least five data points per crystallite were measured. The standard reference materials used for the analysis were diopside (Ca-Kα), corundum (Al-Kα) and magnetite (Fe-Kα). Furthermore, a so-called PRZ matrix correction was applied. Finally, the Fe^{2+}/Fe_{tot} ratio was calculated from the total iron content based on the crystal-chemical formula obtained from microprobe measurements and charge balance considerations (Droop 1987).

Other parts of the pellets were further crushed in an agate mortar. Ten black platy fragments of crystals with largest diameters of about 150 μm were extracted and mounted on the tips of glass fibers with nail hardener. Unit-cell parameters of the crystalline samples at ambient temperature (23 °C) were obtained by single-crystal diffraction (Mo-Kα radiation) using an Oxford Diffraction Gemini R Ultra single-crystal diffractometer. These screening experiments proved the presence of SFCA-II crystals. However, many of the samples were subject to non-merohedral twinning. For more detailed structural investigations of the compound showing a triclinic (pseudo-monoclinic) unit cell, a crystal virtually free from twinning effects was selected. A total of 1178 frames using ω-scans with 0.5 ° scan width per frame and 60 s exposure time covering a full sphere of reciprocal space were collected. Integration and data reduction were performed using the

CrysAlisPro software package (Rigaku Oxford Diffraction 2015) including the corrections for Lorentz- and polarization effects. Furthermore, an empirical absorption correction was applied. Ionic X-ray scattering factors for Ca^{2+}, Al^{3+}, Fe^{3+} and O^{1-} together with real and imaginary coefficients for anomalous dispersion were taken from the International Tables for Crystallography, Vol. C (Wilson 1995). Refinement calculations were performed using the data published by Mumme (2003) as a starting model. For the corresponding least-squares calculations the program SHELXL-97 (Sheldrick 2015) embedded in the WinGX software suite (Farrugia 1999) was employed. In the final stages of calculations, thermal motion of all atoms was modeled with anisotropic displacement parameters. The allocation of different cation species to the octahedral (M) and tetrahedral (T) sites was obtained by a combination of site population refinements allowing for potential Fe ↔ Al or Fe ↔ Ca substitutions under the assumption of (i) the absence of vacancies, (ii) consideration of crystallochemical aspects, e.g. average M-O and T-O bond distances and (iii) charge balance between the cations and anions. More details concerning the analysis of the cation distributions will be given in the discussion section. The refinements converged to a residual of R1 = 0.0349 for 773 parameters and 7406 independent reflections (see Table 1). The largest shift/esd in the final cycle was <0.001. Coordinates, site occupancies and equivalent isotropic displacement parameters of the atoms as well as selected interatomic distances are summarized in Tables 2 and S1. Anisotropic displacement parameters are listed in Table S2. A comprehensive archive of all structural information can be found in the corresponding crystallographic information file (Appendix S3).

Figures showing structural details were prepared with the program VESTA 3 (Momma and Izumi 2011). For the calculations of the difference mean-square displacement parameters the program XtalDraw (Downs and Hall-Wallace 2003) was employed.

Results

Synthesis and chemical composition

After sintering, the pellets showed a pronounced volume reduction. Partially inter-grown black crystals up to 300 μm in diameter embedded in a gray polycrystalline matrix could be observed. Fig. 1 presents a picture of a characteristic part of the sample taken with a digital microscope. Subsequent EMP analysis revealed the presence of at least three phases. The average compositions of the spot analyses for the different phases are summarized in Table 3. Most of the sample consisted of a Si-free SFCA-II-type compound. Furthermore, when normalized to four oxygen atoms per formula unit (p.f.u.) the derived formula for phase 2 pointed to the existence of iron containing krotite ($CaAl_2O_4$). Depending on the normalization, the chemical composition of phase 3 was consistent with (i) extremely Al-rich SFCA-I (for 28 oxygens p.f.u.) or (ii) Fe-containing grossite ($CaAl_4O_7$, for 7

Table 1 Crystal data and structure refinement for $Ca_{2.46}Fe^{3+}_{8.57}Fe^{2+}_{0.52}Al_{5.45}O_{24}$

Empirical formula	$Ca_{2.46}Fe^{3+}_{8.57}Fe^{2+}_{0.52}Al_{5.45}O_{24}$	
Formula weight	2355.06	
Temperature of data collection	23 °C	
Wavelength	0.71073 Å	
Crystal system	Triclinic	
Space group	$P\bar{1}$	
Unit cell dimensions	$a = 10.3016(4)$ Å	$\alpha = 90.062(3)°$
	$b = 10.4656(4)$ Å	$\beta = 89.977(3)°$
	$c = 17.9553(6)$ Å	$\gamma = 109.510(3)°$
Volume	1824.66(12) $Å^3$	
Z	4	
Density (calculated)	4.139 g/cm^3	
Absorption coefficient	8.091 mm^{-1}	
F(000)	2193	
Crystal size	0.037 × 0.067 × 0.120 mm^3	
Theta range for data collection	3.40 to 26.37°	
Index ranges	$\|h\| \le 12$, $\|k\| \le 13$, $\|l\| \le 22$	
Reflections collected	26,695	
Independent reflections	7406 [R(int) = 0.0487]	
Completeness to theta = 26.37°	99.6%	
Refinement method	Full-matrix least-squares on F^2	
Data / restraints / parameters	7406 / 0 / 773	
Goodness-of-fit onF^2	1.111	
Final R indices ($I > 2\sigma(I)$)	R1 = 0.0349, wR2 = 0.0805	
R indices (all data)	R1 = 0.0500, wR2 = 0.0867	
Largest diff. Peak and hole	1.262 and − 1.166 e.$Å^{-3}$	

Table 2 Atomic coordinates, site populations and equivalent isotropic displacement parameters (Å^2) for $Ca_{2.46}Fe^{3+}_{8.57}Fe^{2+}_{0.52}Al_{5.45}O_{24}$. U(eq) is defined as one third of the trace of the orthogonalized U_{ij} tensor. M23 and M24 reside on special Wyckoff-positions 1*d* and 1*c*, respectively. All other atoms in the asymmetric unit are located on general positions. The iron contents on T28 and T29 (Fe(Tot)) represent the sum of Fe^{3+} and Fe^{2+}

	Site populations in (%)	x	y	z	U(eq)
M1	Fe^{3+}: 74.7(6) Al: 25.3(6)	0.25094(7)	0.50012(7)	0.42166(4)	0.0051(2)
M2	Fe^{3+}: 83.6(6) Al: 16.4(6)	0.24999(6)	0.74993(6)	0.98965(3)	0.0043(2)
M3	Fe^{3+}: 87.3(6) Al: 12.7(6)	0.24975(6)	0.24835(6)	0.15861(3)	0.0047(2)
M4	Fe^{3+}: 89.5(6) Al: 10.5(6)	0.74840(6)	0.99833(6)	0.74482(3)	0.0053(2)
M5	Fe^{3+}: 92.8(6) Al: 7.2(6)	0.75075(6)	0.00015(6)	0.41197(3)	0.0055(2)
M6	Fe^{3+}: 45.1(11) Ca: 54.9(11)	0.75438(7)	0.50309(7)	0.74638(4)	0.0067(3)
M7	Fe^{3+}: 64.0(11) Ca: 36.0(11)	0.25151(7)	0.75111(6)	0.15668(3)	0.0067(2)
M8	Ca: 100.0	0.25811(8)	0.48362(8)	0.88923(4)	0.0074(2)
M9	Fe^{3+}: 79.6(6) Al: 20.4(6)	0.73887(7)	0.75450(6)	0.66237(3)	0.0057(2)
M10	Fe^{3+}: 86.6(6) Al: 13.4(6)	0.75032(6)	0.24914(6)	0.49292(3)	0.0055(2)
M11	Ca: 100.0	0.24355(8)	0.01673(8)	0.88937(4)	0.0072(2)
M12	Fe^{3+}: 79.0(6) Al: 21.0(6)	0.76119(7)	0.24453(6)	0.66204(3)	0.0055(2)
M13	Fe^{3+}: 89.8(6) Al: 10.2(6)	0.24978(6)	0.24883(6)	0.50711(3)	0.0056(2)
M14	Ca: 100.0	0.75582(8)	0.73458(8)	0.30497(4)	0.0078(2)
M15	Fe^{3+}: 84.8(6) Al: 15.2(6)	0.50382(6)	0.25456(6)	0.58515(3)	0.0054(2)
T16	Fe^{3+}: 64.5(6) Al: 35.5(6)	0.44226(7)	0.55572(7)	0.57776(4)	0.0043(3)
M17	Ca: 100.0	0.74547(8)	0.26530(8)	0.30535(4)	0.0079(2)
M18	Fe^{3+}: 87.1(6) Al: 12.9(6)	0.26290(6)	0.49587(6)	0.07246(3)	0.0051(2)
T19	Fe^{3+}: 67.4(6) Al: 32.6(6)	0.94154(7)	0.80424(7)	0.99410(4)	0.0045(3)
M20	Fe^{3+}: 85.8(6) Al: 14.2(6)	0.23743(6)	0.00220(6)	0.07328(3)	0.0049(2)
T21	Fe^{3+}: 13.5(5) Al: 86.5(5)	0.95887(10)	0.33279(10)	0.15939(6)	0.0045(4)
T22	Fe^{3+}: 56.2(6) Al: 43.8(6)	0.55659(7)	0.69668(7)	0.99212(4)	0.0040(3)
M23	Fe^{3+}: 87.2(8) Al: 12.8(8)	½	0	0	0.0055(3)
M24	Fe^{3+}: 88.1(8) Al: 11.9(8)	0	½	0	0.0047(3)
T25	Fe^{3+}: 23.7(5) Al: 76.3(5)	0.54303(9)	0.16137(9)	0.16339(5)	0.0038(3)
T26	Fe^{3+}: 19.7(5) Al: 80.3(5)	0.04422(10)	0.91358(10)	0.74505(5)	0.0050(3)
M27	Fe^{3+}: 85.5(6) Al: 14.5(6)	0.99620(6)	0.74678(6)	0.58547(3)	0.0059(2)
T28	Fe(Tot): 89.5(6) Al: 10.5(6)	0.93712(6)	0.05940(6)	0.58110(3)	0.0055(2)
T29	Fe(Tot): 85.5(6) Al: 14.5(6)	0.56248(6)	0.94045(6)	0.58121(3)	0.0057(2)
T30	Fe^{3+}: 8.1(5) Al: 91.9(5)	0.46214(11)	0.58679(11)	0.74935(6)	0.0058(4)
T31	Fe^{3+}: 2.8(5) Al: 97.2(5)	0.53620(11)	0.66886(11)	0.16191(6)	0.0051(4)
T32	Fe^{3+}: 61.4(6) Al: 38.6(6)	0.05726(7)	0.44498(7)	0.57605(4)	0.0044(3)
T33	Fe^{3+}: 3.8(5) Al: 96.2(5)	0.03632(11)	0.41673(11)	0.74522(6)	0.0056(4)
T34	Fe^{3+}: 11.0(5) Al: 89.0(5)	0.54239(10)	0.91679(10)	0.25876(6)	0.0046(4)
T35	Fe^{3+}: 7.3(5) Al: 92.7(5)	0.03717(11)	0.16482(11)	0.83352(6)	0.0050(4)
O1		0.6450(3)	0.3854(3)	0.84070(18)	0.0182(8)
O2		0.6449(3)	0.6455(3)	0.74817(15)	0.0098(6)
O3		0.3960(3)	0.6126(3)	0.66346(15)	0.0084(6)
O4		0.8661(3)	0.1265(3)	0.00476(15)	0.0076(6)
O5		0.6350(3)	0.6262(3)	0.57707(16)	0.0092(6)
O6		0.6416(3)	0.8790(3)	0.66452(18)	0.0170(7)
O7		0.8645(3)	0.3734(3)	0.57679(16)	0.0094(6)
O8		0.6141(3)	0.8742(3)	0.34208(15)	0.0075(6)
O9		0.8545(3)	0.6309(3)	0.65237(16)	0.0107(6)
O10		0.8594(3)	0.1193(3)	0.66426(17)	0.0153(7)
O11		0.6440(3)	0.3698(3)	0.65283(17)	0.0112(7)
O12		0.6109(3)	0.3348(3)	0.18494(15)	0.0086(6)
O13		0.8668(3)	0.8585(3)	0.57849(16)	0.0105(7)
O14		0.3660(3)	0.8563(3)	0.42230(16)	0.0111(7)
O15		0.6413(3)	0.1304(3)	0.74159(17)	0.0138(7)
O16		0.8941(3)	0.1619(3)	0.18227(16)	0.0094(6)
O17		0.6394(3)	0.1257(3)	0.41821(16)	0.0143(7)
O18		0.8686(3)	0.6268(3)	0.50199(16)	0.0089(6)
O19		0.8632(3)	0.8748(3)	0.41799(16)	0.0123(7)
O20		0.1139(3)	0.8740(3)	0.65897(15)	0.0081(6)
O21		0.5947(3)	0.8371(3)	0.18670(15)	0.0124(7)
O22		0.8579(3)	0.8642(3)	0.74533(15)	0.0086(6)
O23		0.6312(3)	0.3739(3)	0.50107(15)	0.0084(6)
O24		0.1155(3)	0.6329(3)	0.57862(15)	0.0084(6)
O25		0.8556(3)	0.3560(3)	0.74607(17)	0.0196(8)
O26		0.1059(3)	0.3888(3)	0.66100(15)	0.0084(6)
O27		0.6170(3)	0.6329(3)	0.42044(15)	0.0082(6)

Table 2 (continued)

Site populations in (%)	x	y	z	U(eq)
O28	0.5965(3)	0.5836(3)	0.22894(16)	0.0103(6)
O29	0.1030(3)	0.3351(3)	0.81033(15)	0.0099(6)
O30	0.3537(3)	0.8778(3)	0.07116(16)	0.0092(6)
O31	0.1169(3)	0.6230(3)	0.92167(15)	0.0069(6)
O32	0.3832(3)	0.8790(3)	0.92075(15)	0.0072(6)
O33	0.8557(3)	0.3777(3)	0.92831(15)	0.0086(6)
O34	0.3660(3)	0.6272(3)	0.99383(15)	0.0080(6)
O35	0.6276(3)	0.8690(3)	0.49160(16)	0.0112(7)
O36	0.8729(3)	0.1307(3)	0.49202(16)	0.0098(6)
O37	0.9141(3)	0.4139(3)	0.23493(16)	0.0137(7)
O38	0.8567(3)	0.6232(3)	0.84254(17)	0.0125(7)
O39	0.8603(3)	0.8696(3)	0.91809(16)	0.0085(6)
O40	0.6219(3)	0.8862(3)	0.99658(15)	0.0076(6)
O41	0.8767(3)	0.6138(3)	0.99905(15)	0.0078(6)
O42	0.8537(3)	0.1098(3)	0.83457(16)	0.0109(7)
O43	0.6446(3)	0.8856(3)	0.83574(16)	0.0089(6)
O44	0.3653(3)	0.3684(3)	0.08402(16)	0.0089(6)
O45	0.6007(3)	0.0875(3)	0.23930(16)	0.0103(6)
O46	0.1025(3)	0.1373(3)	0.91863(15)	0.0086(6)
O47	0.8943(3)	0.9143(3)	0.23472(15)	0.0091(6)
O48	0.6065(3)	0.6417(3)	0.07831(15)	0.0086(6)

oxygens p.f.u.). The latter interpretation was finally corroborated by the PXRD data (see Fig. 2).

Notably, the composition of the Fe-substituted monocalcium aluminate is very close to the one that was observed in the course of a previous study on a mixed crystal in the system $CaAl_2O_4$ – $CaFe_2O_4$ obtained between 1450 and 1350 °C (Kahlenberg 2001) (ICDD entry 04–011-5956). Unfortunately, for Fe-grossite no detailed structural studies have been performed so far and no powder diffraction data are available. When compared with the diffractogram of pure $CaAl_4O_7$ (ICDD entry 04–007-8974, Goodwin and Lindop 1970), however, the corresponding peaks in our sample showed characteristic shifts to lower Bragg angles that could be explained by a partial substitution of Al^{3+} with larger Fe^{3+} cations.

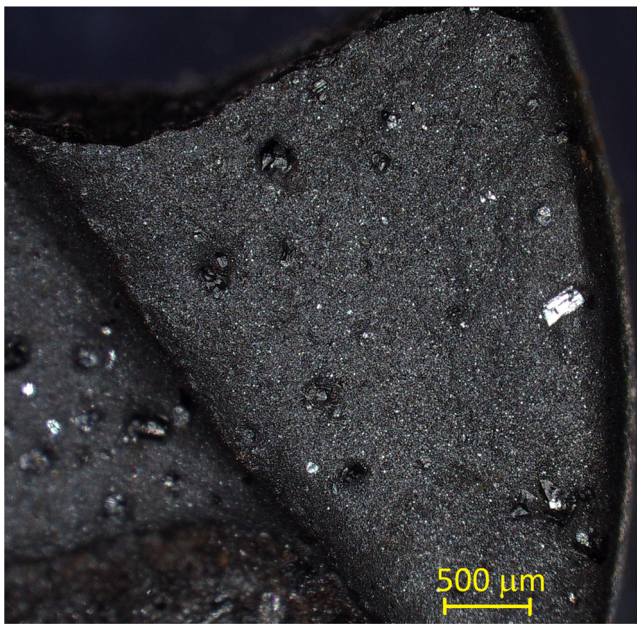

Fig. 1 Picture of a characteristic part of the sample taken with a digital microscope. Partially inter-grown black crystals of SFCA-II up to 250 µm in diameter embedded in a polycrystalline gray matrix can be observed

Crystal structure

As mentioned above, our initial structural investigations were based on the SFCA-II model of Mumme (2003). However, after the first few refinement cycles it became obvious that one of the oxygen positions reported in the previous paper is highly questionable. Actually, the relative z-coordinate of oxygen O15 shifted from 0.705 to about 0.742, corresponding to a displacement of about 0.74 Å. It is noteworthy, that exactly this oxygen atom is involved in the suspicious bond distances that were the starting point for this investigation. Since all other atomic positions could be principally confirmed, we assume that the discrepancy is probably related to transposed digits in Mumme's original publication. In order to facilitate the comparison between both structure determinations we finally decided to use the same numbering for the atoms as in the previous study.

The crystal structure of SFCA-II shows the typical features of the SFCA-family. It can be built from an alternating sequence of two different types of fundamental layers oriented parallel to (100). Layer-type I is solely based on $[MO_6]$-octahedra (M: Ca, Fe^{3+}, Al) forming individual bands (see Fig. 3a). Within a single band the octahedra share common edges. Notably, not all of the potentially available octahedral

Table 3 Summary of the EMP analyses of the phases observed in the sinter pellet. For each phase, the values correspond to the averages of at least five point analyses distributed all over the polished surface. Standard uncertainties are given in parenthesis. The content in Fe^{2+} has been calculated from charge balance considerations (see text)

Phase	Composition
SFCA-II	$Ca_{2.56(3)}\ Al_{5.23(3)}\ Fe^{3+}_{8.76(3)}Fe^{2+}_{0.45}O_{24}$
"Fe-Krotite"	$Ca_{1.01(1)}\ Al_{1.73(3)}\ Fe^{3+}_{0.27(2)}\ O_4$
"Fe-Grossite"	$Ca_{1.04(1)}\ Al_{3.50(4)}\ Fe^{3+}_{0.48(4)}\ O_7$

sites are occupied resulting in the formation of ordered vacancies. The unit cell contains two symmetry equivalent layers of type I located at x ≈ ¼ and ¾, respectively, which are related by an inversion center. Layer-type II, on the other hand, contains $[MO_6]$-octahedra as well as $[TO_4]$-tetrahedra (T: Al, Fe^{3+}, Fe^{2+}) (see Fig. 3b). By corner sharing each $[MO_6]$-group is linked to two adjacent tetrahedra. Hamilton et al. (1989) denominated these $[MT_2O_{12}]$-clusters as "winged octahedra". Linkage between neighboring strips of these moieties is provided by additional $[TO_4]$-tetrahedra arranged in *vierer* single-chains. Within the unit cell, type II slabs are centered at x ≈ 0 and ½. They contain inversion centers and are symmetrically independent from each other.

Alternatively, the crystal structures of SFCA-II can be understood using a modular approach involving the stacking of sequences of "P" and "S" modules that can be imagined as being cut from the well-known pyroxene (P) and spinel (S) structure-types. Indeed, these layers are more or less perpendicular to the sheets of type I and II that have been mentioned above (see Fig. 3). This modular approach has been already outlined in detail in several previous publications for other members of the SFCA-family (see Kahlenberg et al. 2019 and references cited therein). Therefore, we will restrict our description to the key point of this concept. As is obvious from Fig. 4 the whole crystal structure of SFCA-II can be described by the following stacking sequence: <PSPSS>. It can be regarded as a combination of SFCA (<PS>, Hamilton et al. 1989) and SFCA-I (<PSS>, Mumme et al. 1998).

Discussion

Within layer I, different types of M-sites can be distinguished. The positions M8, M11, M14, M17 are completely occupied by calcium cations. To an upper limit of 3 Å, bond distances range between 2.29 and 2.82 Å. Focusing on the six closest neighbors, the coordination environments can be approximated as octahedral. However, for all four M-positions an additional seventh oxygen ligand at larger distances can be found (see Table S1). To facilitate the discussion of the structure, we will neglect these more distant O-atoms and consider all Ca-centered polyhedra as octahedra. Using this approximation, the sequence of five octahedra wide bands in these layers is given in Fig. 3a. Notably, the large pure Ca-polyhedra are exclusively located at the rims of the bands. The sites M1, M2, M3, M4, M5, M9, M10, M12, M13, M15, M18, M20, M23, M24 and M27 are significantly smaller (see Table S1). They show mixed Al – Fe^{3+} distributions with iron occupancies between $x_{Fe} = 0.74$ and 0.92. Their average M-O distances (<M-O>) generally conform to the following linear trend (see Fig. 5):

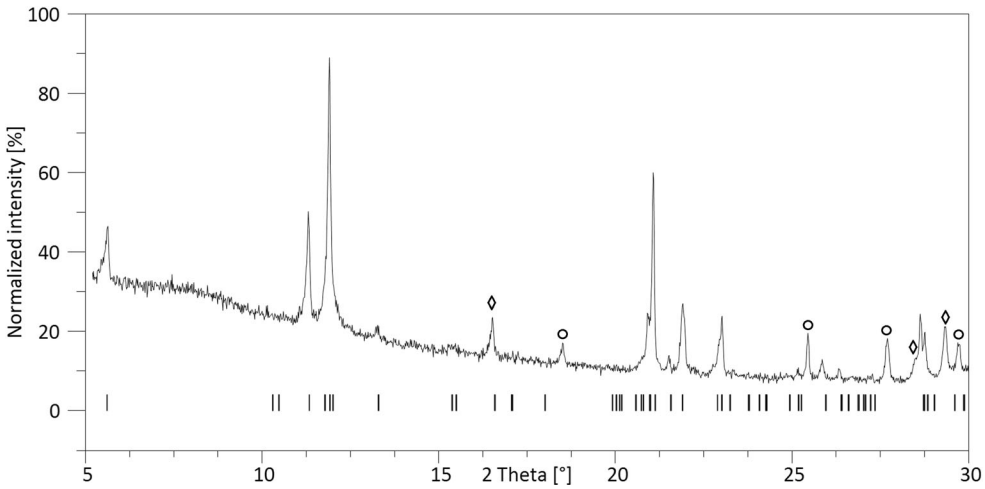

Fig. 2 Part of the powder X-ray diffraction pattern of the sample synthesized at 1300 °C in the range between 5 and 30 ° 2θ. Data were acquired with Co-Kα_1 radiation. Tick marks given in the bottom line correspond to the peak positions of SFCA-II and were generated using the lattice parameters from the present single-crystal structure analysis. Characteristic peaks of Fe-containing $CaAl_2O_4$ and $CaAl_4O_7$ which are not overlapping with reflections from SFCA-II have been marked with circles or diamonds, respectively

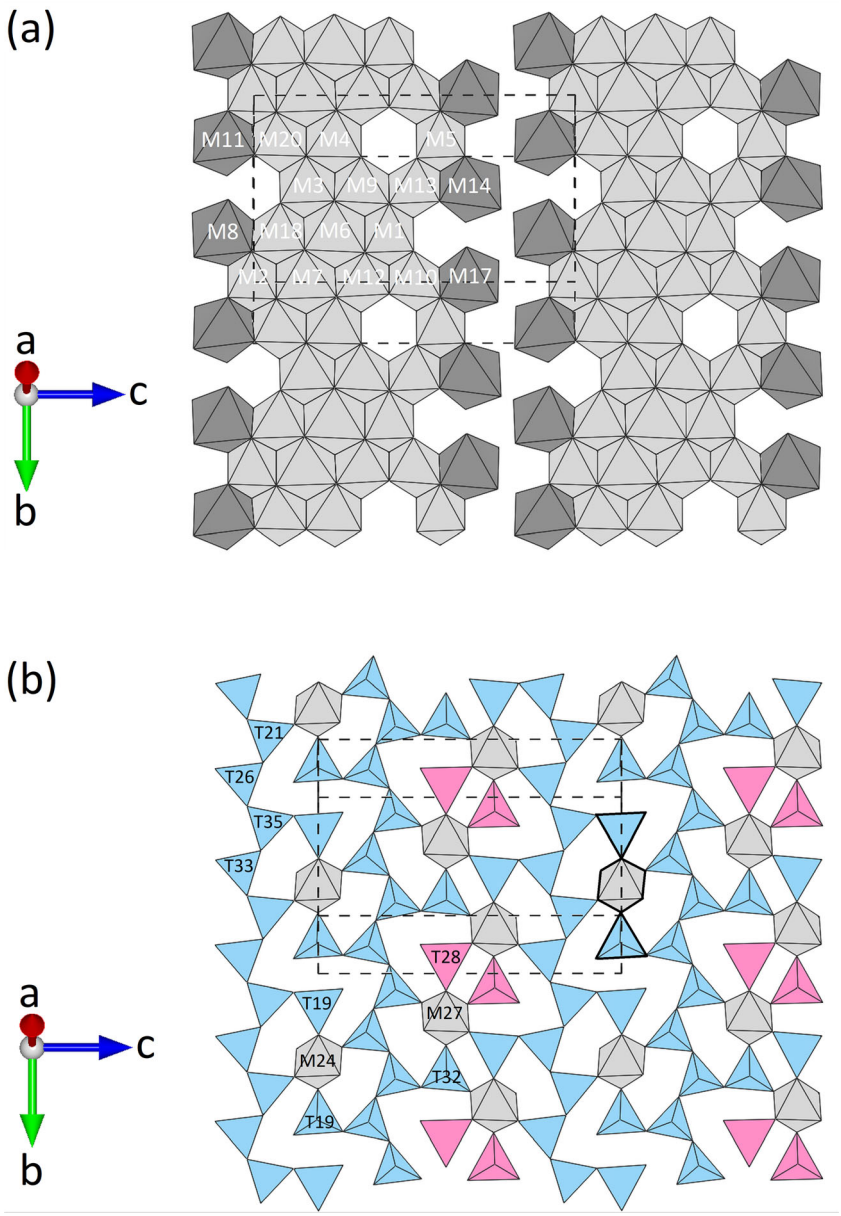

Fig. 3 Fundamental layers observed in SFCA-II. (**a**) Band-like units of octahedra (layer type I, z ≈ ¼) and (**b**) so-called winged-octahedra as well as *vierer* single-chains of tetrahedra (layer type II, z ≈ 0). Layers are shown in projections perpendicular to the sheets. Dark-gray octahedra represent pure [CaO_6]-units, whereas the octahedra about the remaining M-sites are given in light-gray. Blue and red tetrahedra indicate the presence of Fe^{3+} and Fe^{2+}, respectively. For sake of clarity, the contour of a single winged-octahedron is highlighted with bold lines

$$< \mathrm{M{-}O} > = 1.85(2) + 0.21(2) \times x_{\mathrm{Fe}} \left(\mathrm{\AA}\right)$$

Concerning the bond lengths and the polyhedral volumes, the octahedra around M6 and M7 are in between those of the pure Ca-positions and the aforementioned group of smaller octahedra. They occupy the central parts of a single octahedral band. Site population studies point to a simultaneous incorporation of calcium and iron on these two positions. The differences in the ionic radii (Shannon 1976) between Ca^{2+} ($r^{[6]}$ = 1.00 Å) and Fe^{3+} ($r^{[6]}$ = 0.645 Å) are reflected in an increase of the <M-O>-values (M6: 55% Ca / 45% Fe; <M-O> = 2.177 Å and M7: 36% Ca / 64% Fe; <M-O> = 2.124 Å). Alternatively, estimations of the site populations on M6 and M7 were performed using bond valence sum calculations (Wills 2010) with attributing the total iron content to either Fe^{3+} or Fe^{2+}, respectively: M6: 43% Ca / 57% Fe^{3+} (11% Ca / 89% Fe^{2+}); M7: 26% Ca / 74% Fe^{3+} (−7% Ca / 107% Fe^{2+}). Though not matching perfectly, it is obvious that the values for Fe^{3+} are much closer to the ones obtained from the site occupancy refinements. Furthermore, the assumption of ferrous iron on the M7 site results in physically meaningless, i.e. negative percentages for the calcium population. Therefore, it was deemed appropriate to allocate ferric iron to the positions M6 and M7.

The tetrahedra forming the *vierer* single-chains in the layers of type II (T21, T26, T33, T35 and T25, T30, T31, T34, respectively) are aluminum dominated. By contrast, the

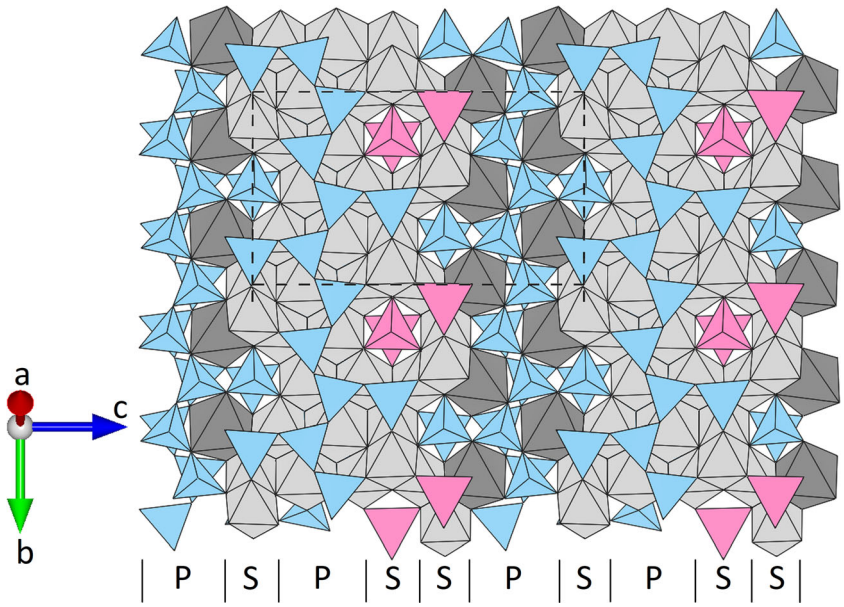

Fig. 4 The crystal structure of $Ca_{2.46}Fe^{3+}_{8.57}Fe^{2+}_{0.52}Al_{5.45}O_{24}$. The sub-division into spinel (S) and pyroxene (P) modules is indicated. The compound corresponds to the <PSPSS> stacking sequence

T-sites belonging to the winged octahedra (T19, T32, T22, T16, T28 and T29) show x_{Fe} values between 0.58 and 0.86. The latter two T-positions exhibiting the highest Fe-contents ($x_{Fe} = 0.82$ and 0.86) deserve special attention. Fig. 6 shows the following linear relation between the average T-O bond distances and the iron concentrations:

$$< T{-}O> = 1.741(2) + 0.169(7) \times x_{Fe} \left(\mathring{A}\right)$$

It seems valid for most of the tetrahedra, however, <T28-O> and <T29-O> deviate significantly from this relation predicting much smaller values compared to those that have been actually determined from crystal structure analysis. Since the incorporation of calcium ions on the T-sites can be excluded for crystallochemical reasons, we interpret this finding as a strong indication that the positions T28 and T29 contain at least some ferrous iron.

Further evidence for the presence of some Fe^{2+} on these two sites comes from detailed analysis of the differences between the anisotropic mean-square displacement parameters of the T and O atoms along the corresponding T-O bonds. When averaged over a complete tetrahedron, these <ΔU>-values can provide insight into static disorder (Bürgi 1984; Kunz and Armbruster 1990). The <ΔU>'s for the tetrahedra around T28 (<ΔU> = 0.011(3) $Å^2$) and T29 (<ΔU> = 0.015(4) $Å^2$) are 2.5 to 5 times larger than the corresponding values for the remaining tetrahedra, which contain only Fe^{3+} and whose thermal vibrations can be approximated as a rigid body motion. Consequently, the significantly increased <ΔU>-values for T28 and T29 would reflect the disorder effects when a comparatively small ion (such as Al^{3+}, $r^{[4]} = 0.39$ Å) shares the same position with a much larger cation (such as Fe^{2+}, $r^{[4]} = 0.63$ Å) (Shannon 1976).

However, presuming that the 1.75 iron atoms in the asymmetric unit residing on the T28 and T29 positions are exclusively ferrous leads to a deficiency of positive charges. In order to achieve charge balance we suggest that - in addition

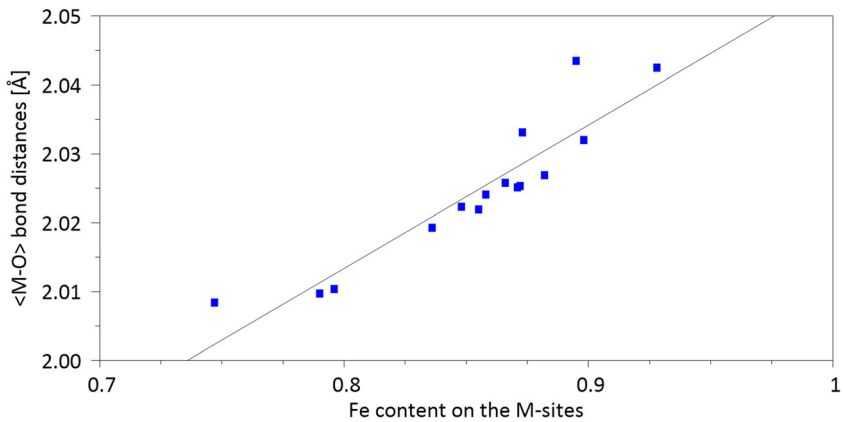

Fig. 5 Evolution of the average <M-O> distances as a function of the Fe content on the octahedral sites

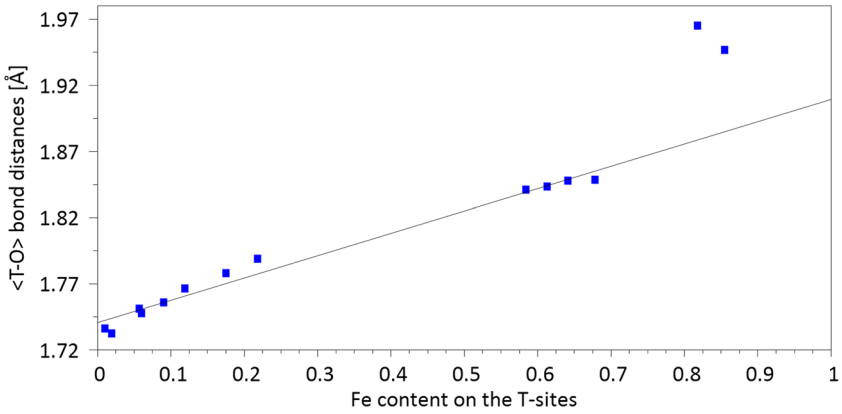

Fig. 6 Evolution of the average < T-O > distances as a function of the Fe content on the tetrahedral sites

to Al^{3+} – both tetrahedral centers contain Fe^{2+} as well as Fe^{3+}. This hypothesis finally results in the following chemical charge neutral formula: $Ca_{2.46}Fe^{3+}_{8.57}Fe^{2+}_{0.52}Al_{5.45}O_{24}$. Of course, we cannot draw any further detailed conclusions about the distribution of the 0.52 ferrous iron cations p.f.u. among the two relevant sites. Furthermore, we cannot preclude with absolute certainty that some minor amounts of Fe^{2+} may be present on M6 and M7, as well. Notably, however, the formula derived by the abovementioned considerations compares rather well with the one that was obtained from microprobe analysis (see Table 3). Differences may be due to spatial variations in chemical composition within the sample. Finally, the results from conventional microprobe analysis may be influenced by systematic errors which can produce inaccurate results unless secondary standards with independently determined Fe^{2+}/Fe_{Total} values are used (Lamb et al. 2012).

A graphical summary of the resulting distributions of the different cation species among the 21 M- and 14 T-sites is shown in Fig. 7. When comparing the distributions with the sizes of the polyhedra it becomes obvious that the small tetrahedra of the *vierer* single-chains surround the very large Ca-centered octahedra and, by contrast, the large ferrous iron containing tetrahedra around T28 and T29 are associated with smaller MO_6-moieties. The $[T28O_4]$- and $[T29O_4]$-tetrahedra reside exactly above and below the vacant octahedral site of the adjacent type I layers, i.e. their basal faces correspond to opposite triangles of the "empty" octahedra. Geometrical requirements concerning the fit between the two layer types seem to influence the cation distributions directly.

Conclusions

The comparison between the compositions of the SFCA-II crystals synthesized at 1290 °C by Mumme (2003) with a $PbO\text{-}Bi_2O_3$ flux by solvent evaporation ($Ca_{2.55}Fe^{3+}_{9.35}Fe^{2+}_{0.45}Al_{4.65}O_{24}$) and our sample ($Ca_{2.46}Fe^{3+}_{8.57}Fe^{2+}_{0.52}Al_{5.45}O_{24}$) shows, that the derived chemical formulas are similar. The differences are primarily related to the Fe^{3+}/Al^{3+} ratios. Furthermore, in both SFCA-II representatives, minor amounts of ferrous iron could be identified.

For the calculation of several quantitative descriptors for the characterization of the degree of similarity between the two crystal structure refinements of SFCA-II - after a correction of the

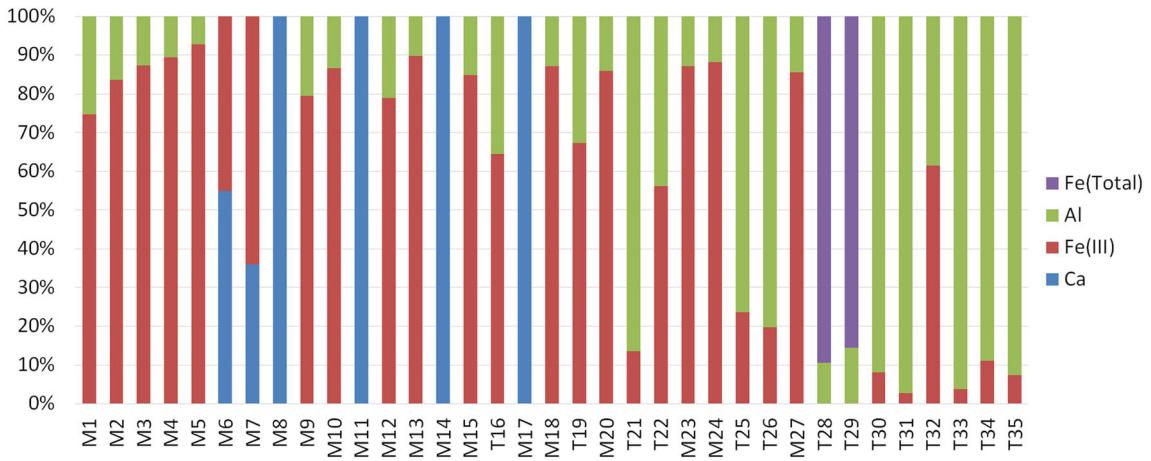

Fig. 7 Bar graph visualizing the cation distributions among the different M- and T-sites

error in the coordinates of the oxygen atom O15 in the previous study - the program COMPSTRU (de la Flor et al. 2016) was used. For the given two structures, the degree of lattice distortion (S), i.e. the spontaneous strain obtained from the eigenvalues of the finite Lagrangian strain tensor calculated in a Cartesian reference system, has a small value of S = 0.0021. Subsequently, the structure data of Mumme (2003) was mapped on the most similar configuration of our analysis. The calculations revealed the following ranges of atomic displacements (in Å) between the corresponding atoms in both refinements: M/T: 0.002–0.076 (arithmetic mean: 0.036) and O: 0.020–0.228 (arithmetic mean: 0.096). The measure of similarity Δ as defined by Bergerhoff et al. (1999) has a value of 0.015. These data clearly indicate, (i) that both crystal structures are isotypic and (ii) that the relative shifts of the oxygen ligands are more pronounced.

Despite the similarity of the atomic coordinates, the results of both refinements differ in terms of the distribution of the calcium and the ferrous iron ions among the M- and T-positions. Mumme (2003) exclusively allocated the Fe^{2+}-ions present in SFCA-II to the M6 site. However, this assumption leaves us with problem that there is no explanation for the significantly increased sizes of the tetrahedra about T28 and T29 – a structural feature that occurred in the former refinement as well. As outlined above, we prefer a solution where ferrous iron is distributed among these two sites. The question, if Fe^{2+} could occur on the M6 and M7 sites as well, cannot be answered with absolute certainty. For the present structure model we refrained from this option.

Notably, a detailed look on the thermal displacement parameters given in Mumme (2003) reveals some problems as well. Many of the isotropic temperature factors have extremely low values. Additionally, a total of 13 U(iso)-values are zero within one standard deviation. This observation could be attributed, for example, to a non-ideal absorption correction, an insufficient data to parameter ratio or errors in site occupancies when mixed cation positions are considered. Thermal parameters are usually strongly correlated with the site occupancies and, therefore, problems with the first set can directly impair the outcome of the cation distributions and vice versa. Since the quality of our data allowed for an anisotropic modeling of the thermal motion for all 83 symmetrically independent atoms and the displacement parameters are generally well behaved, we consider our refinement a significant improvement.

Finally, the linear relationship between the <T-O> -values and the content in Fe^{3+} may be transferred to other SFCA-type compounds for (i) estimation of the Fe^{3+}/Al^{3+} ratios from pure geometrical parameters such as bond distances and (ii) detection of Fe^{2+} on specific T-sites, i.e. in case that stronger deviations from the predicted linear trend line occur.

The results of the previous and the new structural investigations on SFCA-II show that there are still a lot of open questions. First of all, the observed spread in the iron – aluminum ratios in both studies imply the existence of a solid-solution series, the extent of which as a function of (i) temperature, (ii) composition and (iii) oxygen fugacity is not understood so far. Furthermore, very recently Mumme and Gable (2018) reported the existence of a monoclinic polytype of SFCA-II. This observation adds additional complexity but also opens a new field for research activities because the stability of the polytypes has to be considered as well for a comprehensive understanding of the phase evolution. The latter aspect is not only of interest for fundamental research but could also have some practical implications. Actually, industrial sintering is combined with very fast quench rates and this parameter should definitely have an impact on the formation and the frequency distribution of different polytypes in the sinter phases. To the best of our knowledge, this aspect has been completely neglected in the characterization of the products from sinter plants by PXRD. In summary one can say that - despite of many decades of research activities on SFCA's and their relevance for an important industrial process - this class of materials still can present many surprises.

Supplementary Information The online version contains supplementary material available at https://doi.org/10.1007/s00710-020-00730-y.

Acknowledgments We would like to thank Thomas Armbruster for the helpful discussion on the Fe^{2+}/Fe^{3+} problem during the preparation of this manuscript. The paper benefitted from the comments of Tonci Balic-Zunic and a second anonymous reviewer.

Authors' contributions VK conceived and planned the investigation. He performed single-crystal structure analysis and wrote the manuscript with the help of HK. HK carried out the powder diffraction studies. MT performed the EMP analyses. Synthesis experiments were part of BA's bachelor thesis.

Funding Open Access funding provided by University of Innsbruck and Medical University of Innsbruck.

Data availability All primary structural information is included in the corresponding CIF-file that has been uploaded as well.

Compliance with ethical standards

Conflict of interest Not applicable.

Code availability Not applicable

References

Bergerhoff G, Berndt M, Brandenburg K, Degen T (1999) Concerning inorganic crystal structure types. Acta Cryst B 55:147–156

Bürgi HB (1984) Stereochemical lability in crystalline coordination compounds. Trans Am Crystallogr Assoc 20:61–71

De la Flor G, Orobengoa D, Tasci E, Perez-Mato JM, Aroyo MI (2016) Comparison of structures applying the tools available at the Bilbao crystallographic server. J Appl Crystallogr 49:653–664

De Villiers J, Verryn S (2008) Modern X-ray diffraction methods for process optimisation in the minerals industry - case studies. Paper presented at: ICAM 2008. Proceedings of the ninth international congress for applied mineralogy; 2008 Sep 8-10. The Australasian Institute of Mining and Metallurgy, Brisbane, Australia, pp 265–275

Downs RT, Hall-Wallace M (2003) The American Mineralogist Crystal Structure Database. Am Mineral 88:247–250

Droop GTR (1987) A general equation for estimating Fe^{3+} concentrations in ferromagnesian silicates and oxides from microprobe analyses, using stoichiometric criteria. Mineral Mag 51:431–435

Farrugia LJ (1999) WinGX suite for small-molecule single-crystal crystallography. J Appl Crystallogr 32:837–838

Fernandez-Gonzalez D, Ruiz-Bustinza I, Mochon J, Gonzalez-Gasca C, Verdeja L (2017) Iron ore sintering: process. Miner Process Extr Metall Rev 38:215–227

Gates-Rector SD, Blanton TN (2019) The powder diffraction file: a quality materials characterization database. Powder Diffract 34:352–360

Goodwin DW, Lindop AJ (1970) The crystal structure of $CaO{\cdot}2Al_2O_3$. Acta Cryst B 86:1230–1235

Hamilton J, Hoskins B, Mumme W, Borbridge W (1989) The crystal-structure and crystal-chemistry of $Ca_{2.3}Mg_{0.8}Al_{1.5}Si_{1.1}Fe_{8.3}O_{20}$ (SFCA) - solid-solution limits and selected phase-relationships of SFCA in the SiO_2-Fe_2O_3-CaO(-Al_2O_3) system. N Jb Mineral (Abh) 161:1–26

Jankovic A (2015) Developments in iron ore comminution and classification technologies. In: Lu L (ed) Iron ore: mineralogy, processing and environmental sustainability. Woodhead Publishing, Cambridge, pp 250–282

Kahlenberg V (2001) On the Al/Fe substituion in iron doped monocalcium aluminate – the crystal structure of $CaAl_{1.8}Fe_{0.2}O_4$. Eur J Mineral 13:403–410

Kahlenberg V, Krüger H, Goettgens VS (2019) Structural elucidation of triclinic and monoclinic SFCA-III – killing two birds with one stone. Acta Cryst B 75:1126–1136

Kunz M, Armbruster T (1990) Difference displacement parameters in alkali feldspars: effects of (Si,Al) order-disorder. Am Mineral 75: 141–149

Lamb WM, Guillemette R, Pop RK, Fritz SJ, Chmiel GJ (2012) Determination of Fe^{3+}/Fe using the electron microprobe: a calibration for amphiboles. Am Mineral 97:951–961

Merlino S, Zvyagin B (1998) Modular features of sapphirine-type structures. Z Kristallogr 213:513–521

Momma K, Izumi F (2011) VESTA 3 for three-dimensional visualization of crystal, volumetric and morphology data. J Appl Crystallogr 44: 1272–1276

Mumme W (1988) A note on the relationship of $Ca_{2.3}Mg_{0.8}Al_{1.5}Si_{1.1}Fe_{8.3}O_{20}$ (SFCA) with aenigmatite group minerals and sapphirine. N Jb Mineral Mh 8:359–366

Mumme W (2003) The crystal structure of SFCA-II, $Ca_{5.1}Al_{9.3}Fe^{3+}_{18.7}Fe^{2+}_{0.9}O_{48}$ a new homologue of the aenigmatite structure-type, and structure refinement of SFCA-type, $Ca_2Al_5Fe_7O_{20}$. Implications for the nature of the "ternary-phase solid-solution" previously reported in the CaO-Al_2O_3-iron oxide system. N Jb Mineral (Abh) 178:307–335

Mumme WG, Gable RW (2018) Crystal structures of monoclinic variants of two SFCA structure-types containing significant Fe^{2+}: crystal structure of monoclinic SFCA-II, $Ca_{2.6}Fe^{3+}_{8.0}Fe^{2+}_{3.4}Al_4O_{24}$; and proposed structure of monoclinic SFCA-I, ideally, $Ca_2Fe^{2+}_8Fe^{3+}_8Al_4O_{28}$. N Jb Mineral (Abh) 195:89–100

Mumme W, Clout J, Gable R (1998) The crystal structure of SFCA-I $Ca_{3.18}Fe1_{4.66}{}^{3+}Al_{1.34}Fe_{0.82}{}^{2+}O28$, a homologue of the aenigmatite structure type, and Mg-free SFCA, $Ca_{2.45}Fe_{9.04}{}^{3+}Al_{1.74}Fe_{0.16}{}^{2+}Si_{0.6}O_{20}$. N Jb Mineral (Abh) 173:93–117

Nicol S, Chen J, Pownceby M, Webster N (2018) A review of the chemistry, structure and formation conditions of silico-ferrite of calcium and aluminum ('SFCA') phases. ISIJ Int 58:2157–2172

Patrick T, Lovel R (2001) Leaching dicalcium silicates from iron ore sinter to remove phosphorus and other contaminants. ISIJ Int 41: 128–135

Rigaku Oxford Diffraction (2015) CrysAlisPRO, version 1.1713843. Rigaku Oxford Diffraction, Oxford

Shannon RD (1976) Revised effective ionic radii and systematic studies of interatomic distances in halides and chalcogenides. Acta Cryst A 32:751–767

Sheldrick GM (2015) Crystal structure refinement with SHELXL. Acta Cryst C 71:3–8

Van den Berg T, de Villiers J (2008) Improving sampling methodology for the evaluation of fines production at Vanderbijl Park sinter plant, South Africa. Paper presented at: ICAM 2008. Proceedings of the ninth international congress for applied mineralogy; 2008 Sep 8-10. The Australasian Institute of Mining and Metallurgy, Brisbane, Australia, pp 713–717

Webster N, Pownceby M, Madsen I, Kimpton J (2012) Silico-ferrite of calcium and aluminum (SFCA) iron ore sinter bonding phases: new insights into their formation during heating and cooling. Metall Mater Trans B Process Metall Mater Process Sci 43:1344–1357

Wills AS (2010) VaList, version 4.0.7. Program available from www.ccp14.ac.uk. Accessed 1 September 2020

Wilson AJC (ed) (1995) International tables for crystallography, volume C. Mathematical, Physical and Chemical Tables, 1st edn. Kluwer Academic Publishers, Dordrecht, Boston, London

Zöll K, Kahlenberg V, Krüger H, Tropper P (2018) Investigations on FCAM-III ($Ca_{2.38}Mg_{2.09}Fe_{10.61}{}^{3+}Fe_{1.59}{}^{2+}Al_{9.33}O_{36}$): a new homologue of the aenigmatite structure-type in the system CaO-MgO-Fe_2O_3-Al_2O_3. J Solid State Chem 258:307–319

Zvyagin B, Merlino S (2003) The pyroxene-spinel polysomatic system. Z Kristallogr 218:210–220